4D Tomography for neutron depth profiling applications

Neagu, R.; Golenev, S.; Werner, L.; Berner, C.; Gilles, R.; Revay, Z.; Ziegele, L.; Plomp, J.; Märkisch, B.; Gernhäuser, R.

DOI
10.1016/j.nima.2024.169543

Publication date
2024

Document Version
Final published version

Published in
Nuclear Instruments and Methods in Physics Research, Section A: Accelerators, Spectrometers, Detectors and Associated Equipment

Citation (APA)
Neagu, R., Golenev, S., Werner, L., Berner, C., Gilles, R., Revay, Z., Ziegele, L., Plomp, J., Märkisch, B., & Gernhäuser, R. (2024). 4D Tomography for neutron depth profiling applications. *Nuclear Instruments and Methods in Physics Research, Section A: Accelerators, Spectrometers, Detectors and Associated Equipment*, *1065*, Article 169543. https://doi.org/10.1016/j.nima.2024.169543

Nuclear Instruments and Methods in Physics Research A 1065 (2024) 169543

Contents lists available at ScienceDirect

Nuclear Inst. and Methods in Physics Research, A

journal homepage: www.elsevier.com/locate/nima

Full Length Article

4D Tomography for neutron depth profiling applications

R. Neagu [a,*], S. Golenev [a], L. Werner [a], C. Berner [a], R. Gilles [b], Z. Revay [b], L. Ziegele [a], J. Plomp [c], B. Märkisch [a], R. Gernhäuser [a]

[a] TUM School of Natural Sciences, Physics Department, Technical University of Munich (TUM), 85748 Garching, Germany
[b] Forschungs-Neutronenquelle Heinz Maier-Leibnitz, Technical University Munich, 85748 Garching, Germany
[c] Delft University of Technology, Reactor Inst., 2629 Delft, The Netherlands

ARTICLE INFO

Keywords:
Neutron depth profiling
N4DP-instrument
Double-sided silicon strip detector
Self-triggering electronics
FRM II
RID

ABSTRACT

High-rate Neutron Depth Profiling (NDP) is a very efficient and precise probe for studying the evolution of lithium concentration in thin-layer structures, *e.g.*, battery electrodes. NDP is typically limited to a one-dimensional depth analysis summed over the profile area covered by the neutron beam. We developed a detector system based on double-sided silicon strip detectors (DSSSD) with extremely thin and homogeneous entrance windows to provide a new quality of NDP measurements in 3+1 dimensions for the N4DP instrument at the FRM II in Garching, Germany. Using the ^{6}Li(n, α)^{3}H reaction in an experiment conducted at the research reactor in Delft, we achieved a lateral position resolution down to ~100 µm and an energy resolution with $FWHM \approx 10$ keV for the triton particles at energies of 2.7 MeV. High-resolution 3D pictures with a contrast uncertainty < 10% per pixel can be achieved faster than 1 picture per minute. This rate can be adjusted individually for each experiment by sacrificing granularity in the position measurement.

1. Introduction

The neutron depth profiling (NDP) instrument N4DP [1] is situated at the Prompt Gamma Activation Analysis (PGAA) facility [2] of the research reactor FRM II in Garching, Germany. NDP is a sensitive method to extract density profiles of certain nuclides in different host materials [3]. Biersack et al. [4] applied it for lateral localization of neutron-induced reactions. The intercalation of lithium in modern electrode materials and the characterization of thin interphases between the electrolyte and the electrode, named solid electrolyte interphase (SEI), have attracted attention but also demand new detection systems to disentangle the lateral, depth, and temporal variation.

One of the most important NDP application is the investigation of Li-ion batteries [5–7]. Here, the quantitative analysis of the Li-ion homogeneity across the depth is evaluated. One can scan the surface using a narrow, collimated neutron beam to resolve the distribution laterally, as shown in [8]. However, this requires long measurements to collect sufficient statistics at each point. A position-sensitive detector allows us to reduce this to a single measurement, simultaneously collecting data from the entire sample area in parallel.

High-resolution 2D visualization can be achieved using multipixel detectors in a close sandwich geometry [9], where the image is reconstructed from the back-to-back reactions. Due to the compact geometry, the sensors are also irradiated in the neutron beam, getting damaged over time and inducing a substantial background, especially when going to higher neutron fluxes.

Lichtinger et al. [10] and others [11,12] showed that position-sensitive NDP measurements are also possible with commercially available monolithic position-sensitive diodes [13]. Due to pile-up effects and slow detector response, these detectors are unsuitable for the high rates needed for *operando* measurements [14], where batteries are charged and discharged during the measurement.

The main criterion for a well-designed neutron depth profiling detector is a thin and homogeneous dead layer [15], while high detector efficiency, spatial resolution, and high rate capability are also important. Unsegmented detectors based on Si with thin dead layers ≈100 nm [16] are already established and commercially available,[1] as currently used in FRM II. However, highly segmented sensors for better spatial resolution are still being sought for particle detection applications.

This paper presents a newly developed double-sided silicon strip detector (DSSSD) with custom-made low-noise electronics for NDP applications. Two different methods for position reconstruction and their limitations are described in Section 2. The main technological developments of the detector are described in Section 3. A first commissioning experiment using thermal neutrons at the research reactor

* Corresponding author.
E-mail address: robert.neagu@tum.de (R. Neagu).
[1] MICRON Semiconductor Ltd, Sussex, UK

https://doi.org/10.1016/j.nima.2024.169543
Received 11 April 2024; Received in revised form 1 June 2024; Accepted 18 June 2024
Available online 24 June 2024

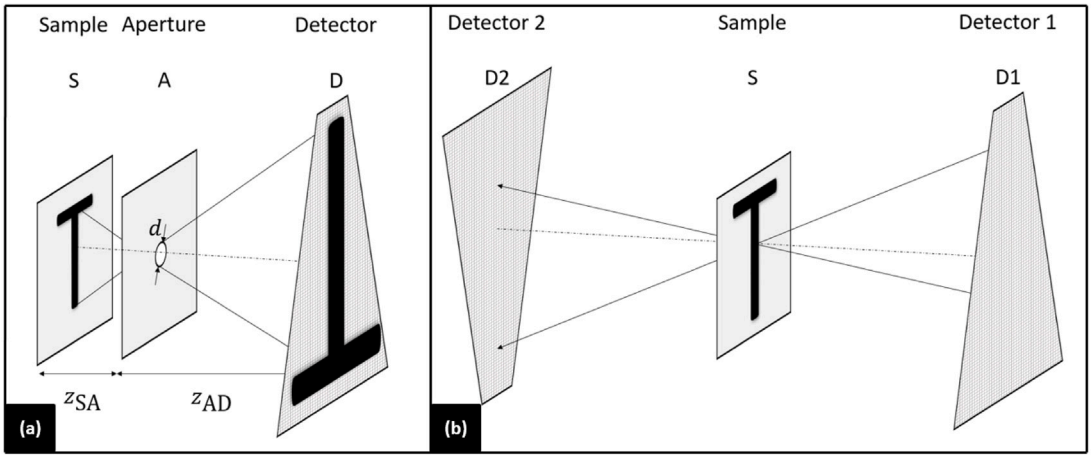

Fig. 1. (a) Camera obscura method. A pinhole aperture A is used to create an inverse image of the sample S on the detector D. Depending on the setup's geometry, this image is also magnified. **(b) Coincidence method.** The origin of the particle reaction signal can be located by using two detectors D_1 and D_2 on each side of the sample.

in Delft, The Netherlands, is described in Section 4 and its results with discussion in Section 5.

2. Lateral scanning methods

To probe the lateral distribution on a target plane, two methods are mainly used: camera obscura and coincidence (Figs. 1a and 1b). The camera obscura method is a single-detector method that uses a pinhole to create an inverse magnified picture on the detector. We define the magnification factor M as the ratio between the distances from the detector to aperture (z_{AD}) and from sample to aperture (z_{SA}): $M = \frac{z_{AD}}{z_{SA}}$. Since the projection of a point through the aperture with the diameter d is a convolution, its magnified image with the size $m = (M+1)\cdot d$ on the detector whose pitch width is p, the achievable resolution is given by the standard deviation s of the trapezoidal distribution [17]:

$$s = \sqrt{\frac{2p^2 + 2p\cdot(m-2p) + (m-2p)^2}{12}}\,. \tag{1}$$

An advantage of this method is the tunability of s at the costs of the field of view. However, a significant disadvantage is the lower geometrical efficiency since the aperture blocks most particles.

The coincidence method is a dual detector method based on the emission of two particles in opposite directions. Using two 2D detectors, we can correlate the two hits and reconstruct the target from the setup. Eq. (1) gives the standard deviation for this method with the particular case $p = m/2$, describing the standard deviation of a triangular distribution.

We can choose one method depending on the sample's thickness, composition, and density. For thicker samples, the ions might lose all of the energy in the sample itself, making it impossible to detect both particles. Therefore, the reconstruction fails in this case. In Table 1, some critical thicknesses are shown exemplarily. The maximum thicknesses allowed for either method are calculated using the WebAtima[2] tool and the SRIM-software [18].

For thin (*i.e.* less than 30 µm) Li-containing samples, this method works only if the α-particles can be detected at both sides. For the ^{10}B(n, α)^{7}Li reaction, the recoil nucleus is heavier, and it thus loses even more energy. Therefore, samples must be thin (as shown in Table 1).

3. Detector and electronics

In this section, we introduce the detector with the corresponding electronics developed for 3 spacial + 1 temporal dimensional (4D) neutron depth profiling.

The 150 µm thick isosceles trapezoid-shaped detector[3] is segmented in 266 horizontal strips on the p-side (Fig. 2a) and 32 fan-out strips on the n-side (Fig. 2b), with lengths ranging from 5.70 cm (major side) to 0.89 cm (minor side) and pitch width of 260 µm for the p-side, and equally sized n-side strips with an average length of 6.89 cm and pitch widths ranging from 265 µm (minor side) to 1766 µm (major side). A pixel on the detector is represented by the overlapped area of one p and one n strip. The detector's trapezoidal shape allows different n strip widths for an adjustable position resolution (at least in one dimension). The trapezoidal shape of the detector is also motivated by the collaborative development of the detector for the HI-TREX upgrade at CERN/ISOLDE [20], where the detectors are arranged spherically to achieve a large solid angle coverage. The outer dimensions of the detector are 60.42 mm on the major side, 10.64 mm on the minor side with the length 71.64 mm and an active area of $A_{\text{eff}} \approx 22.51\,\text{cm}^2$. This is enveloped by a bias ring connected through poly-silicon resistors to each strip with sheet resistances of about 5 kΩ. The bias ring is surrounded by guard rings, which reduce the field strength at the edges [21]. Finally, on the ohmic side, neighboring n^+-contact strips are isolated by the p-stop technique [22], preventing short circuits.

The novelty of this detector is given by an additional oxide layer on the p^+-side between the strips to compensate for inhomogeneities of the ultra-thin (≈150 nm) dead layer. The particles must pass through this passive layer to reach the active volume. In this layer, particles lose a given energy, which raises the detection threshold [23]. These effects are even more pronounced in setups with close geometries, where particles enter the passive layer at skewed angles and travel longer.

We designed a printed circuit board (PCB) with a cut-out for detector emplacement, input and output channels for biasing and testing, and other electronic components, such as temperature sensors and AC coupling. The cut-out is a 1.0 mm deep milling on the back side of the 1.6 mm thick PCB. The detector is glued on top of a 0.30 mm thick silicon frame to remove stress from any thermal expansion. In addition, we glued a 0.38 -mm-thick silicon bar on top to provide stability while bonding the n strips to the electronics. We bonded the 266 p-strips in groups of 2 and with a lower granularity of 3 on the detector border to achieve the maximum number of 128 channels. The front-end electronic is based on application-specific integrated circuits (ASIC) technology using the SKIROC 2A [24] and SKIROC CMS [25] chips. These feature 64 input channels each, a large dynamic charge range from 1/2 MIP (2 fC or ≈ 12500 e$^-$) up to 2000 MIP (8 pC or ≈ $50\cdot10^6$ e$^-$), as well as a

[2] Energy Loss Calculator, developed by the GSI - Available: https://www.isotopea.com/webatima/#!/ (Visited on June 1, 2024)

[3] Made by the sensor supplier CiS Forschungsinstitut für Mikrosensorik GmbH

Table 1
Maximum depth for camera obscura and maximal thickness for coincidence method for different materials. The imaging depth gives the theoretical maximum penetration depth, which one can obtain from the lighter particles of the reaction. In contrast, the reconstruction thickness is the theoretical maximum thickness of the sample to reconstruct the target from both reaction particles, which is given by two times the maximum penetration depth of the heavier ion, *i.e.* the recoiled particle. These values do not take into consideration the electronic offset (energy cutoff) or further energy losses, such as in a Kapton tape, which acts as a separation foil (used, *i.e.*, in [5] to block the α particles).

Host material composition	Reaction of interest	Max. imaging depth [μm]	Max. reconstruction thickness [μm]
Mylar-foil with LiF	^{6}Li(n, α)^{3}H	50.4	16.8
SiG Electrodes (20% Si) [7]	^{6}Li(n, α)^{3}H	90.5	30.4
CoRe HT Alloy [19]	^{10}B(n, α)^{7}Li[a]	4.2	4.8

[a] There are two possible neutron capture reactions for ^{10}B (see www.neutrondepthprofiling.com/reactionsofinterest). Here, we refer to the reaction with the higher energy of the decay particles, *e.g.* the reaction into the ground state of ^{7}Li.

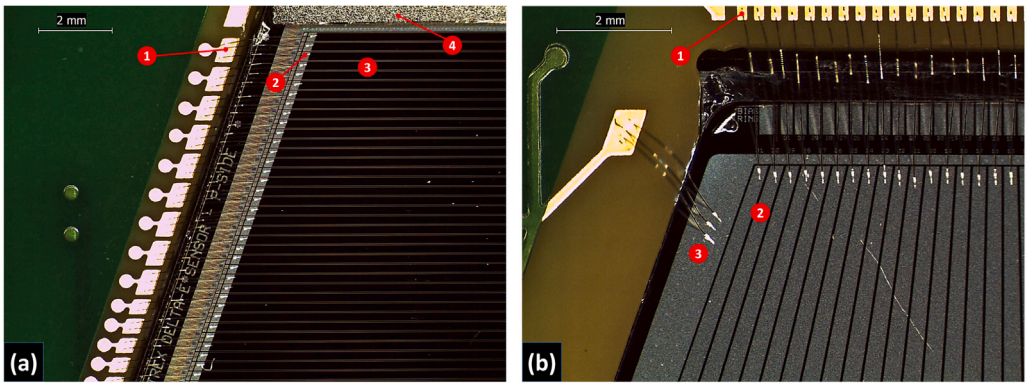

Fig. 2. (a) Detectors *p* **side.** Several parts are labeled: 1. a gold pad that connects three *p* strips together; 2. the DC pad of a *p* side strip that is bonded from; 3. the active *p* side area of the detector; 4. a support bar to keep the detector level when bonding from the *n* side. On the upper part of the detector, we have a lower granularity (three strips together) to match the 266 strips to the 128 channels of the electronics. **(b) Detectors** *n* **side.** Several parts are labeled: 1. gold pads for the *n* side signals; 2. the active *n* side area of the detector; 3. the high voltage area connected to the gold pad by three bonds. The fan-out geometry of the *n* strips is shown.

low equivalent noise charge (ENC < 6 keV for the 2A and < 8 keV for the CMS), individual threshold control and timing output [26]. Each channel of an ASIC consists of several (15 for the 2A and 13 for the CMS) so-called switched-capacitor arrays (SCA) to store the data. After filling up all the CMS SCAs, the data is bunched, and the ASICs are read out. For data controlling and transferring in the front- and back-end electronics, a GEneric Asic Readout (GEAR) board was developed and integrated into the TRB framework of GSI [20,27].

4. Experimental setup and rate considerations

4.1. Detector configuration

We conducted experiments at the Reactor Institute Delft (RID) of the University of Technology Delft to test both methods described in Section 2 with our new detector setup. A vacuum chamber with dimensions (19 × 19 × 110) cm^3 was utilized. To match our technical requirements, we designed a modified lid with feed-throughs for the GEAR boards and vacuum-tight LEMO-connectors.[4] We included a 1.0-mm-thin aluminum window in the lid as an exit to minimize background radiation.

We mounted an aluminum support on the lid, connected by thermal pads[5] to keep our detector setup at a constant temperature, avoiding any drifts of the leakage current worsening the energy resolution [28]. We fixed the detector-PCBs on this support, with heat-conducting pads serving as spacers for isolation and thermal conduction. We denoted the detectors as B and E after the hex code of the distinct GEAR-boards. On average, the DSSSDs were located $\bar{z} \approx 56.0$ mm away from the target.

[4] LEMO SWH.00.250.NTMV
[5] Part number 2617837 from Tru Components

Due to spatial limitations, we arranged the detectors mirrored to the beam axis (as shown in Fig. 3), changing the coordinate system from a left-handed (detector B) to a right-handed (detector E). Consequently, the particles emitted back-to-back reach the two detectors at the same y coordinates. At the same time, they have opposite x coordinates. The target was positioned at the center, in the setup's symmetry point. To ensure uniform neutron illumination, the sample was tilted at an angle $\phi = 45°$ w.r.t. the surface in the horizontal plane, increasing the effective target thickness by $\sqrt{2}$. Additionally, it was tilted at an angle $\theta = 34°$ w.r.t. the vertical plane. For the camera obscura measurement, we added a 2.0-mm-pinhole in front of detector B. We set the magnification ratio for this method to 2.

4.2. Neutron beam and expected reaction rate

The neutron flux profile was a collimated, rectangular beam with a cross-section of 20 × 30 mm^2 with a nominal flux of $\Phi \approx 1.0 \times 10^7$ cm^{-2} s^{-1}, with a wavelength maximum ≈1.8 Å. Therefore, we can use the thermal cross section of $\sigma_{\text{th}} \approx 940$ barn for the ^{6}Li(n,α)^{3}H reaction. To test the rate capability of our system, we needed a count rate ≈500–600 s^{-1}. We achieved this particular rate by modifying the lithium thickness on the substrate, made of a 5-μm-thick Mylar foil. The detection rate R at the detector is given by

$$R = \Phi \cdot \sigma_{\text{th}} \cdot N \cdot \epsilon\,, \tag{2}$$

where Φ is the neutron flux, σ_{th} is the thermal cross section for absorption, N is the total number of target particles (in our case, the ^{6}Li atoms), and $\epsilon \approx 9.23\%$ the average detector acceptance, which is estimated from Monte Carlo simulations.

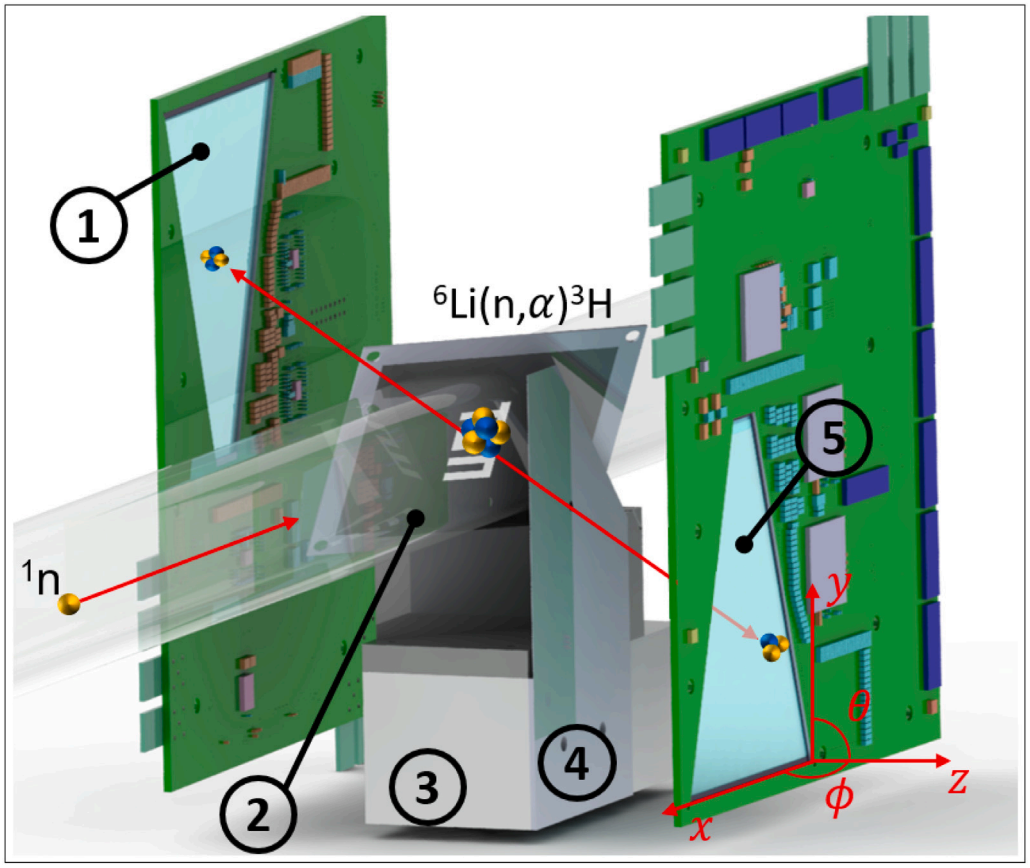

Fig. 3. CAD (3D-view) of the experimental setup. The main parts are labeled: 1. detector E; 2. sample with a TUM pattern; 3. sample support structure; 4. a pinhole aperture fixed to the support structure; 5. detector B. Detector B is located in front of the aperture. The two detectors B and E are mirrored around the vertical plane of the neutron beam axis. The center of the sample is positioned at the symmetry point of the two detectors. The sample is tilted by $\phi = 45°$ in the horizontal plane (xz-plane) and by $\theta = 34°$ in the vertical plane (yz-plane). The neutron beam, denoted with ^{1}n, hits the ^{6}Li target, producing the back-to-back decay of the triton and α particles.

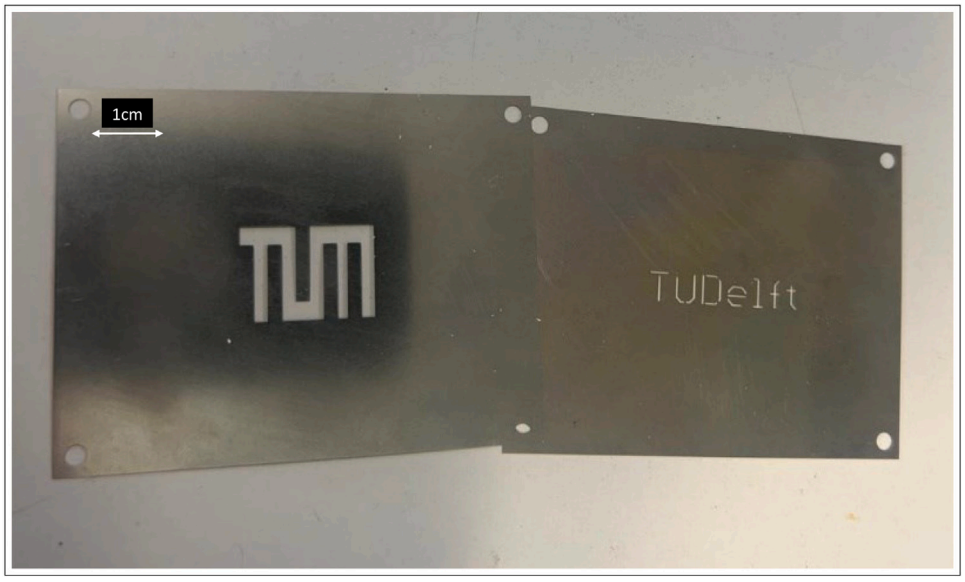

Fig. 4. 100 μm thick masks with different patterns. The TUM and TUDelft logo masks are used to create patterns on both sides of a Mylar foil sample.

Special masks were manufactured[6] (shown in Fig. 4) with individual patterns (a TUM and a TUDelft logo). Then, we vapor deposited highly enriched (~99%) ^{6}LiF through these masks on each side of the 5-μm-thick Mylar film. The vapor deposition was done with an electron beam, which heated the LiF target, accelerating the ions through the mask. This mask was placed between the source and substrate foil attached to an aluminum frame. To achieve the expected rate (we use an average

[6] Laser cut by Becktronic GmbH

Table 2
^{6}Li(n, ^{3}H)^{4}He reaction particles. Rest energies for both particles passing perpendicularly through 5 μm mylar film are listed for comparison.

	^{3}H	α
Initial Energy [MeV]	2.727	2.055
Rest Energy [MeV]	2.547	0.868
$\mathbf{d}E/\mathbf{d}x$ [MeV/(mg/cm^2)]	0.257	1.456

value of $R \approx 550\,\mathrm{s}^{-1}$ for the calculation), we calculate the theoretical areal density of the lithium layer for the TUM logo $\rho_{A,\mathrm{TUM,calc}} = \frac{m}{A_{\mathrm{TUM}}} = \frac{M \cdot N}{A_{\mathrm{TUM}} \cdot N_A}$ by substituting N from Eq. (2):

$$\rho_{A,\mathrm{TUM,calc}} = \frac{M \cdot R}{\Phi \cdot \sigma_{\mathrm{th}} \cdot A_{\mathrm{TUM}} \cdot N_{\mathrm{A}} \cdot \epsilon} \approx 16.15\,\frac{\mu\mathrm{g}}{\mathrm{cm}^2}\,, \tag{3}$$

where $M = 25.01\,\frac{\mathrm{g}}{\mathrm{mol}}$ is the molar mass of enriched ^{6}LiF, N_{A} is the Avogadro constant and $A_{\mathrm{TUM}} \approx 1.63\,\mathrm{cm}^2$ is the surface area of the target TUM logo (covered with ^{6}LiF).

While vapor depositing LiF, for the TUM logo, we measured a thickness of $\rho_{A,\mathrm{TUM,meas}} \approx (15.0 \pm 1.0)\,\mu\mathrm{g/cm}^2$ and for the Delft logo we measured $\rho_{A,\mathrm{TUDelft,meas}} \approx (10.3 \pm 1.0)\,\mu\mathrm{g/cm}^2$ (with an area $A_{\mathrm{TUDelft}} \approx 0.31\,\mathrm{cm}^2$). We observed the rates to be $529\,\mathrm{s}^{-1}$ for the TUM logo and $90\,\mathrm{s}^{-1}$ for the TUDelft logo. This matches our expected rate values, calculated using the measured areal density and inserted in Eq. (3).

4.3. Synchronization and time drift

Since independent self-triggered electronics operate each detector, the clocks of the different FPGAs are not synchronized, which means that we obtain asynchronous timestamps. Therefore, to correlate the data collected from various sensors, we need to adjust the trigger times for each entry based on the synchronization time $t_{\mathrm{sync},i}$ (with $i = B, E$ for different detectors) distributed to each GEAR board using a custom built trigger device.

In this time correction process, the readout signal from detector B is used as the time updater, *i.e.*, the synchronization time of each FPGA is updated whenever a readout signal is received from detector B. Then, for detector E, the data is corrected by subtracting the synchronization time difference $\Delta t_{\mathrm{sync}} = t_{\mathrm{sync},B} - t_{\mathrm{sync},E}$ between the boards. The trigger times of detector B remain uncorrected since it acts as a master board. The time difference represents the clock drift of the FPGA clocks. We obtain correlated events by adjusting the trigger times on both detectors. (If we had a master clock shared by both FPGAs, such a correction would be unnecessary.)

As described in Section 3, the SKIROC CMS ASIC collects data for up to 13 events. After these events, we read out the data, and here, our system stops acquiring for the dead time of $t_d \approx 7\,\mathrm{ms}$. The rates obtained from above are the instantaneous rates, determined from such bundled events.

5. Results

In this section, we describe the results of the two methods (described in Section 2) used with the experimental setup shown in Fig. 3. We used a 5-μm-thick Mylar film with the two patterns (described in Section 4.2).

We used the coincidence method without an aperture to achieve the most precise target reconstruction and a high rate. Since the TUM logo side of the target has a larger area and mass thickness, and the substrate foil blocks the α particles from the opposite side, we observed more events on detector B facing the TUM logo. We observe $\sim 3.8 \cdot 10^6$ events in detector B and $\sim 2.5 \cdot 10^6$ events in detector E, as expected. The rates calculated for each detector in Section 4.2 are given by the corrected counts in either sensor divided by the measurement time (~2.5 h).

Fig. 5 shows the energy distribution on the p strips after the energy calibration for detector E in the measurement without the aperture. We calibrated the channels with a linear fit by assuming that the ^{3}H peak and the α peak are situated at 2.727 MeV and 2.055 MeV, respectively, and the pedestal (*i.e.* electronic noise) as the origin. We calculated the energy of the ^{3}H coming from the other side of the film (in Table 2) and checked the correct calibration. We observe a broadening of this ^{3}H peak, explained by a larger effective thickness.

We observe a bend for the p side on the upper part of the detector. This effect is due to the tilting of the sample and its height, which is almost aligned with the detector's top side. At the very top of the detector, the smallest value of $|\theta|$ exceeds 0. Consequently, the peak is skewed towards lower energies at the top of the detector. We have a maximum angle of $\theta \approx 48°$, corresponding to an energy loss for the ^{3}H of about 274 keV.

Table 3
Calculated positional resolutions for both methods in comparison. For the pinhole we used $d = 2\,\mathrm{mm}$ and a magnification of $M = z_{\mathrm{AD}}/z_{\mathrm{SA}} = 2$. The uncertainties were calculated using the error propagation of Eq. (1). The following uncertainties were assumed: $\Delta d = 0.05\,\mathrm{mm}$, $\Delta z_{A-D} = 1\,\mathrm{mm}$, $\Delta z_{S-A} = 1\,\mathrm{mm}$, $\Delta p = 0.04\,\mathrm{mm}$. The Δp was used for varying x and y coordinates. To obtain approximately the same resolution for the camera obscura method as for the coincidence method in the same setup, an aperture of $d \approx 0.25\,\mathrm{mm}$ had to be used.

Resolution	Coincidence	Camera Obscura
$s_{x,\mathrm{min}}$ [mm]	0.108 ± 0.016	1.657 ± 0.082
$s_{x,\mathrm{max}}$ [mm]	0.721 ± 0.016	1.324 ± 0.076
$s_{y,\mathrm{min}}$ [mm]	0.212 ± 0.016	1.589 ± 0.082
$s_{y,\mathrm{max}}$ [mm]	0.318 ± 0.016	1.524 ± 0.081

5.1. Coincidence method

To reconstruct the image, we use the known setup geometry coincident data of the two detectors. First, we define the coordinate system in which we calculate the sample plane and trajectories. We define the origin $(0, 0, 0)$ in the lower right corner of detector B together with the axes, as shown in Fig. 3. Then, we determine the plane equation $Ax + By + Cz + D = 0$ at the sample from the 3D CAD model using three points. Each coincident event is represented by a trajectory defined by the centers of the two pixels the ions hit. The intersection point of this vector with the calculated plane gives the event's origin. Uncertainties arise from the pixel size, as shown in Table 3, which also changes over the trapezoidal detector.

As a result, we could reconstruct both patterns shown in Fig. 6. For these pictures, we used energy filters for the two detectors and both particles with $2000 < E_\alpha < 2100\,\mathrm{MeV}$ and $2650 < E_{\mathrm{t}} < 2750\,\mathrm{MeV}$. Note that for the vector reconstruction, we used the angle of $\phi = 1.5°$ at which the detectors are tilted towards the target as a minor correction.

5.2. Camera obscura

To construct a camera obscura-like setup, we used an aperture of 2 mm between the sample and the detector B at a distance of $z_{\mathrm{AD}} = 37.26$ mm from the detector. This allows for an inverse projection of the target onto the detector as explained in Section 2. By correlating the events obtained from the front and back strips of the DSSSD, we can reconstruct the pattern, as shown in Figs. 7 and 8. We cut all the background events for these images with $E < 2.0$ MeV for better image clarity. As mentioned above, the TUM logo faced detector B, while the TUDelft logo on the other side of the sample faced detector E with no aperture in front of it. Although both sensors ideally detect particles from both sides, we deliberately set the threshold so that the β background from the aluminum surrounding was minimized and the α particles originating from the other side were not seen. We calculated the energy loss of each particle through the 5-μm Mylar film, as shown in Table 2.

The 2D image in Fig. 7 shows all the particles above 2 MeV from the sample on detector B. By rotating the sample around two different

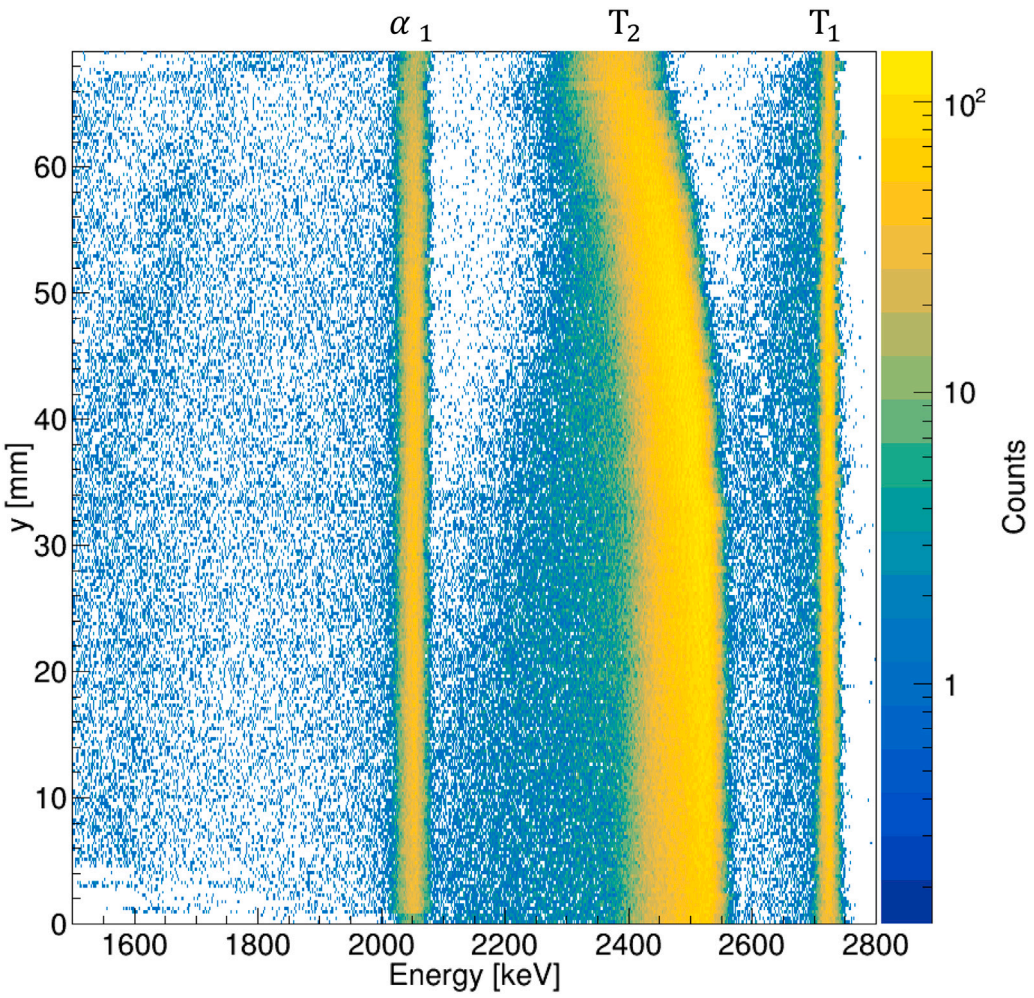

Fig. 5. Y position versus the energy distribution for detector E. On this plot, we can identify the reaction particles for the front side of detector E. Triton and α particles (T_1 and α_1) can be seen at $E_{T_1} \approx 2.727\,\text{MeV}$ and $E_{\alpha_1} \approx 2.050\,\text{MeV}$, respectively. We also observe the triton peak from the other side (T_2). A clear bending and broadening of this signal is observed at energies $\approx 2500\,\text{MeV}$ due to the effectively thicker substrate the particles have to penetrate, which scales with $1/\theta$.

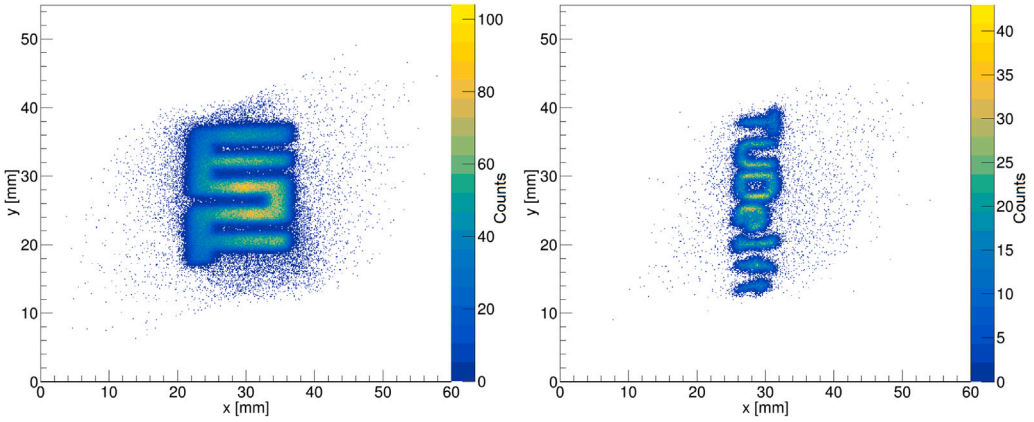

Fig. 6. Reconstructed TUM and TUDelft patterns. Using the coincidence method described in Section 2, both sides of the 5-µm-thick Mylar foil are reconstructed. We applied energy filters to both particles to obtain clear images and reconstructed the images from the vectors intersecting the sample plane.

axes, the resulting image appears tilted, and the magnification varies along the logo. In Fig. 8, a 3D plot of the same image is shown, with different energies for the α and triton particles. Furthermore, we see a ghost image of the ^{3}H particles from the other side of the sample, which is bent towards lower energies at larger y positions, as explained in Fig. 5. Due to the small aperture, the camera obscura method cannot resolve the TUDelft pattern.

Looking at the coincidence of the events on the two detectors, which also crossed the pinhole, we observe a "virtual" image on detector E (Fig. 9). This image has a magnification of $M \approx 4$, as expected from the geometry. If we look at the same events on detector B, we still observe a magnification of $M \approx 2$ as for the image in Fig. 7. However, only a part of the image, which fits within the boundaries of detector E, is visible. Due to the mirrored setup around the center of the target, we observe

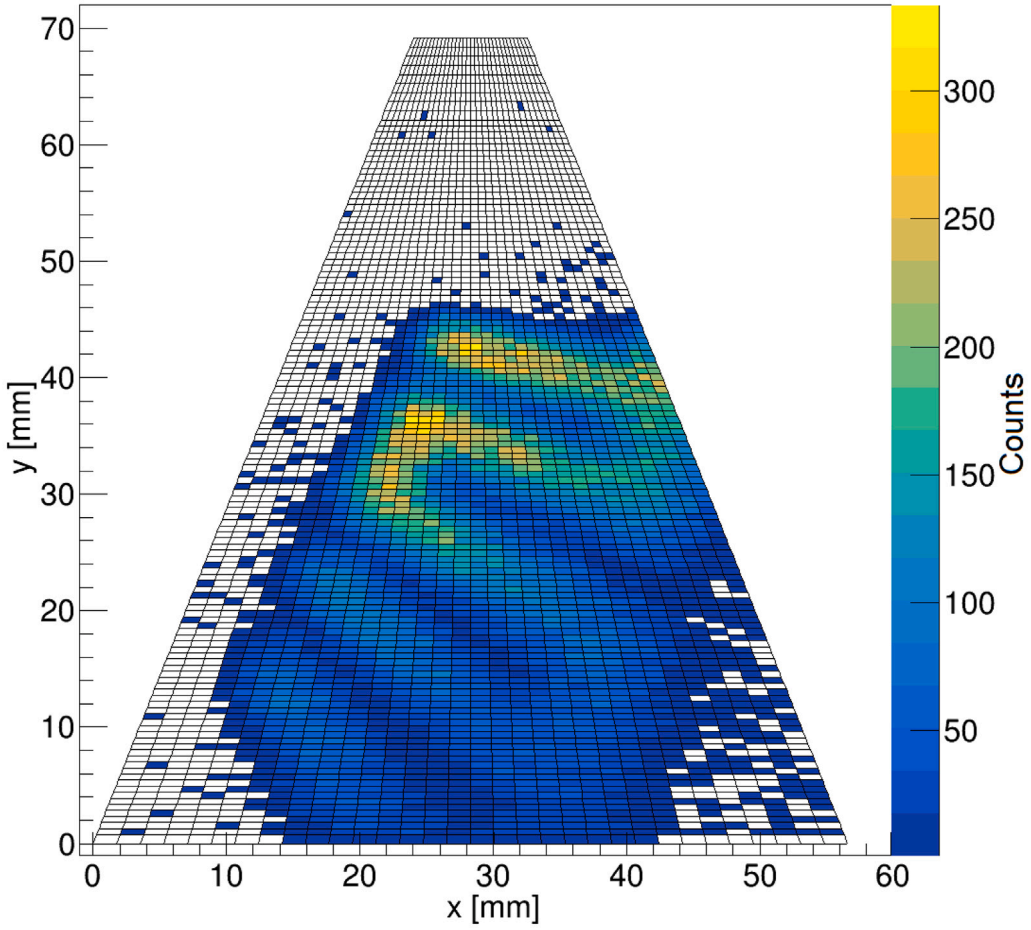

Fig. 7. 2D image using the camera obscura method. Correlated events with energies above 2 MeV detected by the front and back strips of detector B are shown. We used a pinhole with a diameter of $d = 2$ mm between detector B and the sample. The observed shift of the TUM logo can be attributed to the fact that the sample was off-center in the experimental setup. Moreover, tilting the image results from tilting the sample in two directions.

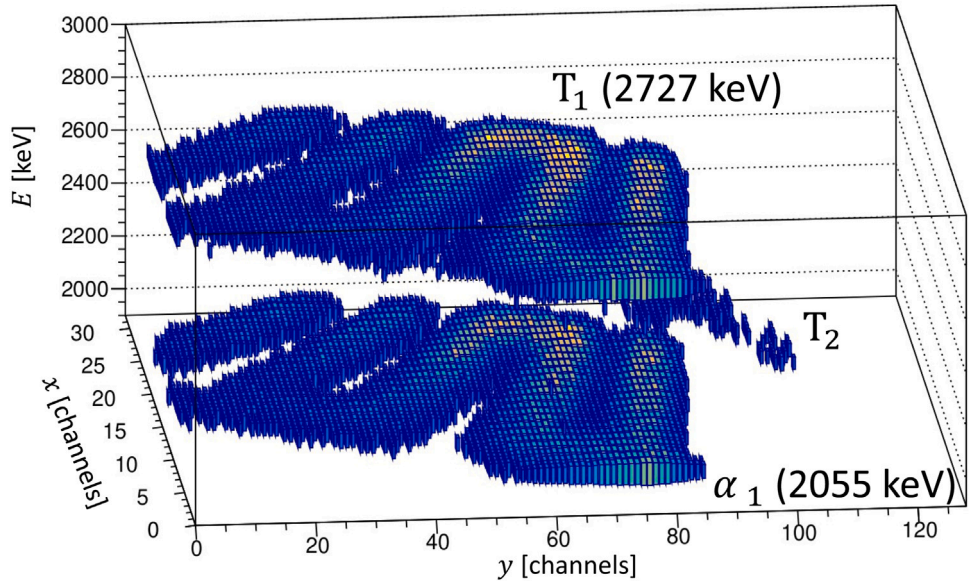

Fig. 8. 3D image for detector B. The x- and y-axes in the graph represent the strip numbers of the detectors. The vertical axis corresponds to the deposited energy of the particles. To improve the visibility of the image, we removed events below 2 MeV. We observe two patterns for the two particles at 2.7 MeV, and 2.0 MeV. Additionally, we see a ghost image at around 2.5 MeV from the triton particles originating from the other side of the sample.

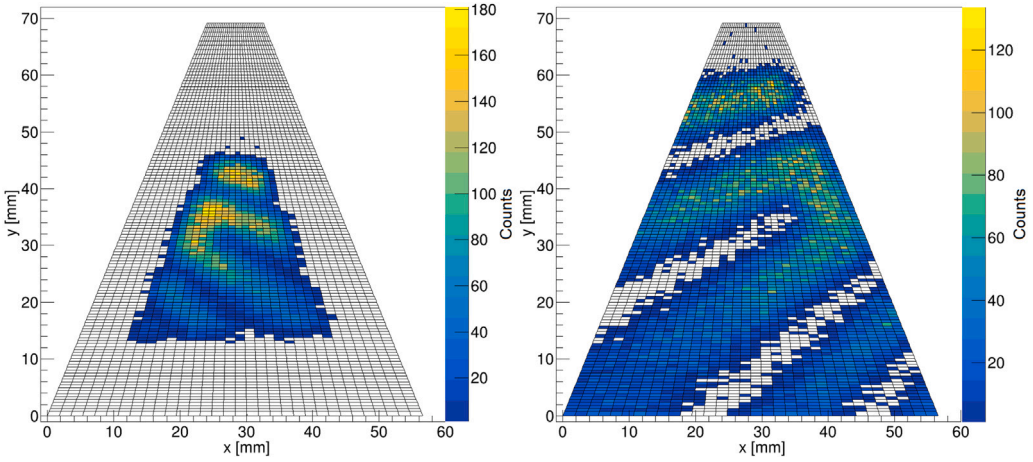

Fig. 9. "Virtual" 2D image of the TUM logo. Only the coincident events are shown. On the left-hand side, the image shows the detector B with a magnification of 2. On the right-hand side, the "virtual" picture on detector E is magnified by four. Additionally, we see opposite x coordinates due to the mirrored setup.

a correlation of the events on the y-axis between the two detectors but an anti-correlation on the x-axis.

5.3. Detector benchmark

To highlight the performance of our system, we have performed a benchmark analysis of our detector across its position, time, and depth resolution. This allows us to assess the detector's performance in a four-dimensional context.

5.3.1. Position resolution

As explained in Section 2, each sample point appears on the detector with the magnified size m and is uniformly distributed. We define the resolution as the standard deviation of the convolution of the pinhole and the pitch size p. For $m \neq p$, the convolution is given by a trapezoidal distribution. The standard deviation for the trapezoidal distribution is given in Eq. (1). For the coincidence method, the resolution is also defined by the convolution of two pitches from both detectors. Since the pitches now have the same size p, the convolution is described by a triangular distribution with the standard deviation of:

$$s_{\mathrm{x,y}} = \frac{p_{\mathrm{x,y}}}{\sqrt{6}}\,. \tag{4}$$

Applying Eq. (1) for p with varying sizes of x and y, we obtain the standard deviations for both methods, as listed in Table 3. The minimum and maximum values for y are given by the different groupings of p strips (2 or 3). For the x values, we used the pitch widths at the bottom and top of the detector.

5.3.2. Depth resolution

For the energy resolution affecting the depth resolution, we use a single channel projection (shown in Fig. 10) of one SCA of detector E without an aperture to avoid any calibration issues. The best possible energy resolution is thus obtained from the ^{3}H peak of the thinner TUDelft logo. We get the full width half maximum ($FWHM$) from a Gaussian fit $FWHM = 2\sqrt{2\ln 2}\cdot s_{\mathrm{E}} \approx 2.3548 \cdot s_{\mathrm{E}} \approx 10\,\mathrm{keV}$.

5.3.3. Temporal resolution

For temporal resolution, we define different time regimes for which we determine their uncertainties: intrinsic, integral, and statistical limits for a 2D image, as discussed below. For a rapidly evolving system, it is essential to measure it at least once in the time interval without any significant change to avoid the aliasing effect (described by the Nyquist–Shannon sampling theorem [29,30]).

Intrinsic and Integral Limits

In single-event cases, where only the energy and timings of single events are essential, we define a temporal resolution constrained by the 200-MHz trigger clock and the switching time between the SCAs. Therefore, the time resolution for single events is roughly 70 ns.

Since we estimated the dead time of our system to be $t_d \approx 7$ ms due to its bunched data stream, this limits the maximum time resolution of any periodic signal. If an infinitesimally small change occurs faster than twice the dead time of our system (aliasing), we cannot tell anything about the evolution. The maximum detection rate that we can achieve is then given by the number of SCAs (13 for the CMS, after which we have a readout) divided by the dead time t_d. Thus, $R_{\mathrm{max}} \approx 2000\,\mathrm{s}^{-1}$.

Statistical Lower Limit

To obtain significant statistics for depth profile histograms (1D), we calculate a minimum time $\Delta T_{\mathrm{min,1D}}$ that we must measure at the maximum rate R_{max}. Here, we define good statistics as the uncertainty of the channels, being $1/\sqrt{N}$ for the number of events N, as 10%. So we need about $N \approx 100$ counts, so that $\Delta N/N \approx \sqrt{N}/N \approx 10\%$. We must also consider the dead time that occurs every 13 events per pixel, so the total dead time $\Delta T_d = t_d \cdot n_{\mathrm{pixel}} \cdot N/13$, with n_{pixel} being the total number of pixels. Since for 1D depth profiling, we assume the whole detector as one pixel, we estimate a $\Delta T_{\mathrm{min,1D}} = N/R_{\mathrm{max}} \cdot n_{\mathrm{pixel}} + \Delta T_d \approx 100\,\mathrm{ms}$.

Now, to obtain a meaningful 3D image on the detector, we also need to consider the area or the number of pixels of the detector hit, which is 4096 pixels for the entire detector. Dividing this by the effective area of the detector gives us $4096/A_{\mathrm{eff}} \approx 1.82\,\frac{\mathrm{pixel}}{\mathrm{mm}^2}$. Assuming a typical NDP sample with a size $\approx 10 \times 10\,\mathrm{mm}^2$ and a magnification of 2, the image is displayed on the detector over ~ 364 pixels. Now, assuming the same maximum rate R_{max} for all pixels, to get the same uncertainty for a 3D histogram, we need $\Delta T_{\mathrm{min,3D}} \approx 37\,\mathrm{s}$, which gives us a lower time limit for an *operando* type of measurement at the achievable positional resolution.

6. Summary and outlook

In summary, we present a DSSSD with a custom-made, self-triggering, time-stamping readout system that can be used for NDP experiments, such as *operando* measurements in 3 + 1D to explore batteries. The resolution of the 2D detector system was determined.

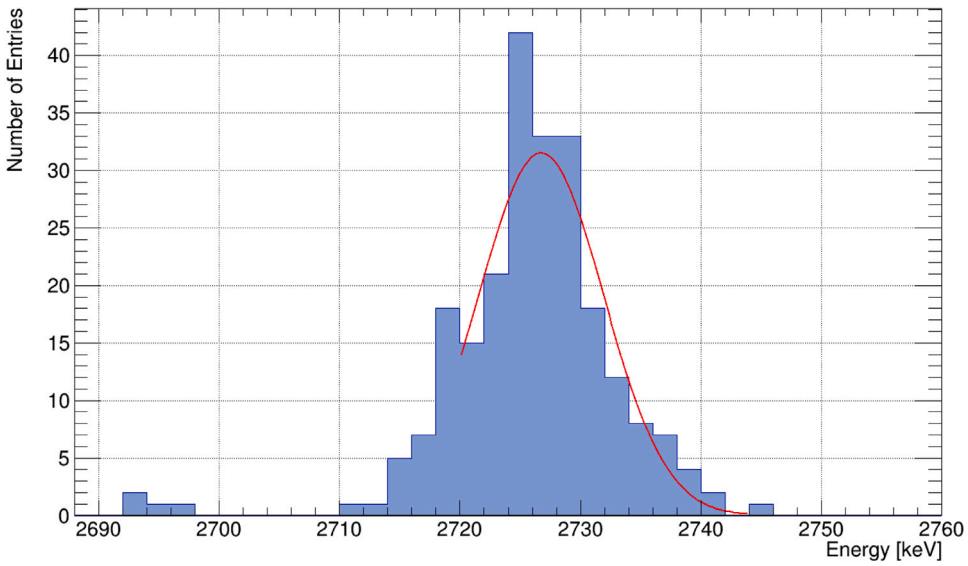

Fig. 10. **^{3}H-peak from the TUDelft logo on detector E.** We fit the ^{3}H peak with a Gaussian distribution and obtain the standard deviation of the energy $s_E \approx 4$ keV corresponding to the depth of $\Delta x \approx 70$ nm for ^{6}LiF. The standard deviation of the energy loss in a 10.3 µg/cm^2 ^{6}LiF layer is of the order of $s_E \approx 1$ keV and has been neglected for this calculation. Only the response at channel #47, SCA #0, was used for this figure.

This versatile setup can be used in different geometries to accommodate different samples. Depending on the application, the position resolution, count rate, and evolution monitoring could be individually optimized.

Assuming a cold neutron beam with the temperature of $T_{cold} \approx T_{th}/10$ and flux of $\Phi = 5\times10^{10}$ cm^{-2} s^{-1}, which is expected at the N4DP instrument at the FRM II, and a cross-section of $\sigma_{cold} \approx \sigma_{th}\cdot\sqrt{10}$, we can roughly estimate the measurement time for the same 3D depth profiles we presented in this paper. The geometric efficiency of the N4DP instrument is estimated to be two times lower than that of the Delft setup, *i.e.* $\epsilon_{N4DP} \approx 4.9\%$. The reconstructed 3D images were obtained in ~2.5 h. With the neutron beam at the FRM II, we reach the readout rate limit of the system, and the same images can be obtained in ~40 min.

To improve the rate for the camera obscura method, one can use a so-called coded mask with a pattern A (which can also be random [31]) instead of a pinhole [32]. This creates a convoluted picture $(S \circledast A)$ of multiple pinholes of the mask on the detector. To obtain the original image S, a de-convolution algorithm G, with $A \circledast G = \delta$, is required [33]. A major advantage of this method is the increased size of the pinholes, resulting in higher rates on the detector. Since the number of pinholes on the coded mask is optimal for signal-to-noise ratio (SNR) of about 1/7 of its area [34] (for 64 pixels with hole sizes of 2×2 mm^2), we expect an increase of 30 in the count rate compared to a 2-mm pinhole. We are currently investigating the applicability of the coded mask technique to a typical NDP geometry.

CRediT authorship contribution statement

R. Neagu: Writing – original draft, Methodology, Investigation, Formal analysis, Data curation, Conceptualization. **S. Golenev:** Visualization, Software, Investigation, Formal analysis, Data curation. **L. Werner:** Writing – review & editing, Investigation. **C. Berner:** Writing – review & editing, Investigation. **R. Gilles:** Writing – review & editing. **Z. Revay:** Writing – review & editing. **L. Ziegele:** Methodology. **J. Plomp:** Resources, Conceptualization. **B. Märkisch:** Writing – review & editing, Supervision, Resources, Funding acquisition. **R. Gernhäuser:** Writing – review & editing, Validation, Supervision, Project administration, Funding acquisition, Formal analysis, Conceptualization.

Declaration of competing interest

The authors declare that they have no known competing financial interests or personal relationships that could have appeared to influence the work reported in this paper.

Data availability

Data will be made available on request.

Acknowledgments

The authors would like to thank Michael Thijs and Raymon Bresser for their help on-site at the research reactor in Delft and for making various mechanical parts for the experiment. We would also like to thank the CiS Forschungsinstitut für Mikrosensorik GmbH for its efficient and close cooperation in developing the detector. The authors thank Ralf Lang and Sonja Winkler from the Department of Physics at the Technische Universität München (TUM) for their assistance with the experimental setup and the bonding of the detectors. Special thanks are also due to Stéphane Callier for providing us with the CMS chips and helping us to understand them better.

The authors acknowledge the financial support of the German Federal Ministry of Education and Research (BMBF), with project numbers 05K16WO1, 05K19WO8, and 05P21WOCI1.

References

[1] L. Werner, M. Trunk, R. Gernhäuser, R. Gilles, B. Märkisch, Z. Révay, The new neutron depth profiling instrument N4DP at the Heinz Maier-Leibnitz Zentrum, Nucl. Instrum. Methods Phys. Res. A 911 (2018) 30–36, http://dx.doi.org/10.1016/j.nima.2018.09.113.

[2] Z. Révay, P. Kudějová, K. Kleszcz, S. Söllradl, C. Genreith, In-beam activation analysis facility at MLZ, Garching, Nucl. Instrum. Methods Phys. Res. A 799 (2015) 114–123, http://dx.doi.org/10.1016/j.nima.2015.07.063.

[3] M. Trunk, M. Wetjen, L. Werner, R. Gernhäuser, B. Märkisch, Z. Révay, H. Gasteiger, R. Gilles, Materials science applications of Neutron Depth Profiling at the PGAA facility of Heinz Maier-Leibnitz Zentrum, Mater. Charact. 146 (2018) 127–134, http://dx.doi.org/10.1016/j.matchar.2018.09.030.

[4] J. Biersack, D. Fink, J. Lauch, R. Henkelmann, K. Müller, An instrument for lattice location studies of light impurity atoms by means of (n, α)-reactions, Nucl. Instrum. Methods Phys. Res. 188 (2) (1981) 411–419, http://dx.doi.org/10.1016/0029-554X(81)90522-X.

[5] M. Wetjen, M. Trunk, L. Werner, R. Gernhäuser, B. Märkisch, Z. Révay, R. Gilles, H.A. Gasteiger, Quantifying the distribution of electrolyte decomposition products in silicon-graphite electrodes by neutron depth profiling, J. Electrochem. Soc. 165 (10) (2018) A2340, http://dx.doi.org/10.1149/2.1341810jes.

[6] M. Wetjen, M. Trunk, L. Werner, H.A. Gasteiger, R. Gernhäuser, R. Gilles, B. Märkisch, Z. Révay, Monitoring the lithium concentration across the thickness of silicon-graphite electrodes during the first (de-)lithiation, J. Electrochem. Soc. 166 (8) (2019) A1408, http://dx.doi.org/10.1149/2.0581908jes.

[7] E. Moyassari, L. Streck, N. Paul, M. Trunk, R. Neagu, C.-C. Chang, S.-C. Hou, B. Märkisch, R. Gilles, A. Jossen, Impact of silicon content within silicon-graphite anodes on performance and Li concentration profiles of Li-Ion cells using neutron depth profiling, J. Electrochem. Soc. 168 (2) (2021) 020519, http://dx.doi.org/10.1149/1945-7111/abe1db.

[8] Y. He, R.G. Downing, H. Wang, 3D mapping of lithium in battery electrodes using neutron activation, J. Power Sources 287 (2015) 226–230, http://dx.doi.org/10.1016/j.jpowsour.2015.03.176.

[9] I. Tomandl, J. Vacík, Y. Mora Sierra, C. Granja, V. Kraus, High resolution imaging of 2D distribution of lithium in thin samples measured with multipixel detectors in sandwich geometry, Rev. Sci. Instrum. 88 (2) (2017) 023706, http://dx.doi.org/10.1063/1.4977217, arXiv:https://pubs.aip.org/aip/rsi/article-pdf/doi/10.1063/1.4977217/13571350/023706_1_online.pdf.

[10] J. Lichtinger, R. Gernhäuser, A. Bauer, M. Bendel, L. Canella, M. Graw, R. Krücken, P. Kudejova, E. Mützel, S. Ring, D. Seiler, S. Winkler, K. Zeitelhack, J. Schöpfer, Position sensitive measurement of lithium traces in brain tissue with neutrons, Med. Phys. 40 (2) (2013) 023501, http://dx.doi.org/10.1118/1.4774053.

[11] E. Portenkirchner, G. Neri, J. Lichtinger, J. Brumbarov, C. Rüdiger, R. Gernhäuser, J. Kunze-Liebhäuser, Tracking areal lithium densities from neutron activation – quantitative Li determination in self-organized TiO2 nanotube anode materials for Li-ion batteries, Phys. Chem. Chem. Phys. 19 (2017) 8602–8611, http://dx.doi.org/10.1039/C7CP00180K.

[12] J. Schoepfer, R. Gernhäuser, S. Lichtinger, A. Stöver, M. Bendel, C. Delbridge, T. Widmann, S. Winkler, M. Graw, Position sensitive measurement of trace lithium in the brain with NIK (neutron-induced coincidence method) in suicide, Sci. Rep. 11 (1) (2021) 6823, http://dx.doi.org/10.1038/s41598-021-86377-x.

[13] M. Lindroos, Ö. Skeppstedt, A position sensitive photon detector used as a charged particle detector, Nucl. Instrum. Methods Phys. Res. A 306 (1) (1991) 225–228, http://dx.doi.org/10.1016/0168-9002(91)90325-K.

[14] F. Linsenmann, M. Trunk, P. Rapp, L. Werner, R. Gernhäuser, R. Gilles, B. Märkisch, Z. Révay, H.A. Gasteiger, A liquid electrolyte-based lithium-ion battery cell design for operando neutron depth profiling, J. Electrochem. Soc. 167 (10) (2020) 100554, http://dx.doi.org/10.1149/1945-7111/ab9b20.

[15] R. Downing, G. Lamaze, J. Langland, S. Hwang, Neutron depth profiling: overview and description of NIST facilities, J. Res. Natl. Inst. Stand. Technol. 98 (1) (1993) 109, http://dx.doi.org/10.6028/jres.098.008.

[16] O. Tengblad, U. Bergmann, L. Fraile, H. Fynbo, S. Walsh, Novel thin window design for a large-area silicon strip detector, Nucl. Instrum. Methods Phys. Res. A 525 (3) (2004) 458–464, http://dx.doi.org/10.1016/j.nima.2004.01.082.

[17] R.N. Kacker, J.F. Lawrence, Trapezoidal and triangular distributions for Type B evaluation of standard uncertainty, Metrologia 44 (2) (2007) 117, http://dx.doi.org/10.1088/0026-1394/44/2/003.

[18] J.F. Ziegler, M. Ziegler, J. Biersack, SRIM – The stopping and range of ions in matter (2010), Nucl. Instrum. Methods Phys. Res. B 268 (11) (2010) 1818–1823, http://dx.doi.org/10.1016/j.nimb.2010.02.091, 19th International Conference on Ion Beam Analysis.

[19] D. Mukherji, R. Gilles, L. Karge, P. Strunz, P. Beran, H. Eckerlebe, A. Stark, L. Szentmiklosi, Z. Mácsik, G. Schumacher, I. Zizak, M. Hofmann, M. Hoelzel, J. Rösler, Neutron and synchrotron probes in the development of Co–Re-based alloys for next generation gas turbines with an emphasis on the influence of boron additives, J. Appl. Crystallogr. 47 (4) (2014) 1417–1430, http://dx.doi.org/10.1107/S1600576714013624.

[20] C. Berner, L. Werner, R. Gernhäuser, T. Kröll, HI-TREX—A highly integrated transfer setup at REX-(HIE)ISOLDE, Nucl. Instrum. Methods Phys. Res. A 987 (2021) 164827, http://dx.doi.org/10.1016/j.nima.2020.164827.

[21] L. Evensen, A. Hanneborg, B.S. Avset, M. Nese, Guard ring design for high voltage operation of silicon detectors, Nucl. Instrum. Methods Phys. Res. A 337 (1) (1993) 44–52, http://dx.doi.org/10.1016/0168-9002(93)91136-B.

[22] R. Richter, L. Andricek, T. Gebhart, D. Hauff, J. Kemmer, G. Lutz, R. Weiss, A. Rolf, Strip detector design for ATLAS and HERA-B using two-dimensional device simulation, Nucl. Instrum. Methods Phys. Res. A 377 (2) (1996) 412–421, http://dx.doi.org/10.1016/0168-9002(96)00257-4, Proceedings of the Seventh European Symposium on Semiconductor.

[23] U. Bergmann, H. Fynbo, O. Tengblad, Use of Si strip detectors for low-energy particles in compact geometry, Nucl. Instrum. Methods Phys. Res. A 515 (3) (2003) 657–664, http://dx.doi.org/10.1016/j.nima.2003.07.016.

[24] S. Callier, F. Dulucq, C.d. Taille, G. Martin-Chassard, N. Seguin-Moreau, SKIROC2, front end chip designed to readout the Electromagnetic CALorimeter at the ILC, J. Instrum. 6 (12) (2011) C12040, http://dx.doi.org/10.1088/1748-0221/6/12/C12040.

[25] J. Borg, S. Callier, D. Coko, F. Dulucq, C.d. Taille, L. Raux, T. Sculac, D. Thienpont, SKIROC2 CMS an ASIC for testing CMS HGCAL, J. Instrum. 12 (02) (2017) C02019, http://dx.doi.org/10.1088/1748-0221/12/02/C02019.

[26] C. Berner, C. Berger, S. Bishop, M. Böhmer, R. Gernhäuser, S. Hellgartner, R. Lang, L. Werner, S. Winkler, A high density readout system for TREX at MINIBALL, Verh. Dtsch. Phys. Ges. (2017).

[27] W. Krzemien, I. Frohlich, M. Kajetanowicz, K. Korcyl, J. Michel, M. Palka, P. Salabura, C. Schrader, P. Skott, H. Strobele, J. Stroth, A. Tarantola, M. Traxler, R. Trebacz, The TRB for HADES and FAIR experiments at GSI, 2008, arXiv:0810.4723.

[28] H. Spieler, Semiconductor detector systems, in: Series on Semiconductor Science and Technology, Oxford University Press, 2005, p. 489.

[29] H. Nyquist, Certain topics in telegraph transmission theory, Trans. Am. Inst. Electr. Eng. 47 (2) (1928) 617–644, http://dx.doi.org/10.1109/T-AIEE.1928.5055024.

[30] C.E. Shannon, Communication in the presence of noise, Proc. IRE 37 (1) (1949) 10–21, http://dx.doi.org/10.1109/JRPROC.1949.232969.

[31] K. McMillan, P. Marleau, E. Brubaker, Random mask optimization for fast neutron coded aperture imaging, Sandia j. manuscript (2015) Not yet accepted for publication.

[32] E. Caroli, J. Stephen, G. Di Cocco, L. Natalucci, A. Spizzichino, Coded aperture imaging in X-and gamma-ray astronomy, Space Sci. Rev. 45 (3–4) (1987) 349–403, http://dx.doi.org/10.1007/BF00171998.

[33] R. Accorsi, R.C. Lanza, Coded aperture fast neutron analysis: latest design advances, AIP Conf. Proc. 576 (1) (2001) 491–494, http://dx.doi.org/10.1063/1.1395356.

[34] A. Talebitaher, P.M. Shutler, S.V. Springham, R.S. Rawat, P. Lee, Coded aperture imaging of alpha source spatial distribution, Radiat. Meas. 47 (10) (2012) 992–999, http://dx.doi.org/10.1016/j.radmeas.2012.07.016.